Phase transformation-induced TGO rumpling failure of an AlCoCrFeNi high-entropy alloy after isothermal oxidation at 1200 °C

DOI:
10.1016/j.scriptamat.2023.115817

Document Version
Accepted author manuscript

Phase transformation-induced TGO rumpling failure of an AlCoCrFeNi high-entropy alloy after isothermal oxidation at 1200 °C

Aihui Huang [a], Ling li [a], Xuanzhen Liu [a], Han Zhang [a], Xiancheng Zhang [b], Jie Lu [a*], Ying Chen [c, d*], Xiaofeng Zhao [a]

[a] Shanghai Key Laboratory of Advanced High-Temperature Materials and Precision Forming, School of Materials Science and Engineering, Shanghai Jiao Tong University, Shanghai, 200240, China

[b] Key Laboratory of Pressure Systems and Safety, Ministry of Education, School of Mechanical and Power Engineering, East China University of Science and Technology, Shanghai, 200237, China

[c] Department of Materials, The University of Manchester, Manchester M13 9PL, United Kingdom

[d] The Henry Royce Institute, The University of Manchester, Manchester M13 9PL, United Kingdom

Abstract:

We compare the oxidation behavior of two AlCoCrFeNi-based high-entropy alloys (HEAs) at 1200 °C. The thermally grown oxide (TGO) on an AlCoCrFeNi HEA undergoes significant surface rumpling, which causes TGO cracking and spallation. However, a similar HEA with a lower Cr content, $AlCoCr_{0.8}FeNi$, shows no TGO rumpling or failure even after 1000 h oxidation. Our analysis suggests that TGO rumpling on the AlCoCrFeNi HEA is predominantly driven by the body-centered cubic (BCC) to tetragonal Cr-rich σ phase transformation within the Al-depleted layer during cooling. A reduction of the Cr content in the HEA or fast water quenching prevents the

* Corresponding authors:
Jie Lu (lu-jie@sjtu.edu.cn)；Ying Chen (ying.chen-2@manchester.ac.uk).

phase transformation and, therefore, TGO rumpling. The findings in this study provide scientific guidance for designing more durable, oxidation-resistant AlCoCrFeNi HEAs and coatings.

Keywords: High-entropy alloy; Phase transformations; Static oxidation; Scale adhesion.

NiCoCrAlY alloys are widely used as the bond coat material in thermal barrier coatings (TBCs) due to their good oxidation resistance at high temperatures [1-2]. Such application depends on the ability to form a slow growing, stable and adherent alumina-base thermally grown oxides (TGO). Minor additions of reactive elements (RE) such as Y and Hf, are always doped the bond coats to improve the TGO adhesion and reduce the TGO growth rate [3-4]. However, conventional NiCoCrAlY bond coats cannot provide sufficient oxidation resistance at temperatures exceeding 1100 ℃, due to fast TGO growth rate and degradation of interfacial adhesion [5]. Consequently, there is an urgent demand for developing new bond coat materials with higher temperature capability (e.g., 1200 ℃), which meets the requirement for the increasing operating temperatures of advanced TBCs [6].

In recent years, high-entropy alloys (HEAs) have gained significant research attentions due to their unique composition, microstructure and exceptional material properties [7-11]. Among these HEA systems, numerous studies have investigated mechanical, electrical, thermal, corrosion and oxidation properties of the $Al_xCoCrFeNi$ HEA system [12-16], providing valuable insights into the potential applications of $Al_xCoCrFeNi$ HEA alloys in various fields. We have reported that RE-doped equimolar AlCoCrFeNi alloy and coating exhibit lower oxidation rates and stronger TGO adhesion than conventional NiCoCrAlYHf at 1100 ℃, which are attributed to the nano-sized coherent microstructure of AlCoCrFeNi HEA [17-19]. These results suggest that RE-doped equimolar AlCoCrFeNi HEA has great potential for the bond coat application in TBCs. However, up to now, the oxidation behavior and failure mechanisms of equimolar AlCoCrFeNi HEA at higher temperature (e.g.,1200 ℃) have been seldom reported.

It is worth noting that reducing the Cr content can inhibit the formation of the Cr-rich detrimental σ phase at high temperature (above 1100 ℃) in the equimolar AlCoCrFeNi HEA, which could maintain its oxidation resistance at 1200 ℃ [20-22]. In this contribution, two HEAs, including AlCoCrFeNi and $AlCoCr_{0.8}FeNi$, are designed to investigate their oxidation behavior at 1200 ℃. Minor Y and Hf are doped into the two HEAs for improving the TGO adhesion [3-4]. The TGO growth and microstructures of the alloys are analyzed in detail to clarify the oxidation behavior of the two HEAs at 1200 ℃.

The AlCoCrFeNi (named HEA1) and $AlCoCr_{0.8}FeNi$ alloys (named HEA2) with minor addition of Y(0.025 at%) and Hf (0.025 at%) were manufactured by arc-melting high-purity constitutional elements (≥99.9%) in water-cooled copper molds. The as-casted ingots were homogenized at 1200 ℃ for 48 h under an argon atmosphere. After that, the ingots were cut into cuboid samples with a dimension of 10 × 10 × 2.5 mm^3 using a precision cut-off machine (Accutom 5, Struers). The sample surfaces were progressively ground on sandpapers with descending grit size to a 5000-grit finish. The samples were then isothermally oxidized in a chamber furnace at 1200 °C in laboratory air and removed from the furnace after the required oxidation time, followed by fan-assisted cooling to ambient temperature.

The microstructure of the alloys was analysed by scanning electron microscopy (SEM, Mira3, Tescan) and scanning transmission electron microscopy (STEM, Talos F200X G2, Thermo Fisher Scientific, USA) fitted with an energy-dispersive X-ray spectroscopy (EDS) system. TEM samples were prepared using a focused ion beam (FIB, GAIA3, Tescan, Czech) and analsysed using transmission kikuchi diffraction (TKD) in the Mira3 SEM to map the phase distribution with a step size of 10 nm. The phase structures of the alloys were identified using X-ray diffraction (XRD,Bruker D8 ADVANCE). The surface roughness of the TGO was measured by an optical profilometer (Zegage™, Zygo, USA) with × 10 lens (Nikon Corporation) and 800 × 800 μm^2 scanning area. A high temperature differential scanning calorimeter (DSC, Germany) was used to analyze the phase transformation of the alloys from room

temperature to 1500 ℃.

The XRD result shows that HEA1 consists of A2 (disordered BCC) and B2 (ordered BCC) phases (**Fig. 1a**). The microstructure of HEA1 exhibits two distinct regions (**Fig. 1b**): the bright region (**Fig. 1c**, B2 precipitates within the A2 matrix) and the dark region (**Fig. 1d**, A2 precipitates within the B2 matrix). The formation of those regions is attributed to the spinodal decomposition process during homogenization at 1200 ℃ [23]. STEM-EDS mapping reveals that the B2 phase is rich in AlNi (dark contrast), while the A2 phase is abundant in CoCrFe (bright contrast) (**Fig. 1e-g**). The chemical compositions of A2 and B2 phases are summarized in **Table. 1**. HEA2 has a similar A2/B2 microstructure with minor FCC precipitates at the grain boundaries (**Fig. 1h-k**). Since Cr acts as a BCC phase stabilizer, reducing the Cr content in HEA2 destabilizes the BCC phase and results in the formation of FCC phase in the alloy [24].

Fig. 2 shows the surface and cross-sectional morphology of HEA1 after 50 h oxidation at 1200 ℃. The TGO formed on the HEA1 exhibits significant rumpling with spallation (**Fig. 2a-b**). TGO rumpling is further confirmed by the surface roughness measurement (R_q=1.94 μm) (**Fig. 2c**). The distribution of Y/Hf-rich oxides at TGO grain boundaries suggests that the dynamic segregation of RE ions occurs during TGO growth, driven by the oxygen potential gradient across the TGO (**Fig. 2d**) [25]. In addition, the clear TGO imprints on the exposed metal surface indicate that no imperfections (e.g., pores) are formed at the TGO/HEA1 interface (**Fig. 2e**). Apart from the surface rumpling of TGO, the Al-depleted layer underneath the TGO (~2.1 μm in thickness) also rumples concurrently, thus causing the interface rumpling (**Fig. 2f-g**). According to the SEM-EDS mapping (**Fig. 2h**), the TGO is exclusive Al_2O_3. The Al-depleted layer shows a dual-phase microstructure that comprises continuous σ matrix and nanoscale BCC precipitates, as confirmed by the TKD analysis (**Fig. 2i**).

Fig. 3 shows the surface and cross-sectional morphology of HEA2 after 50 h and 1000 h oxidation at 1200 ℃. The TGO shows little surface rumpling after 50 h oxidation. A flat Al-depleted layer with a single-phase structure is formed underneath the TGO (**Fig. 3a**). Moreover, the TGO thickness (~2.3 μm) of HEA2 is similar to that of HEA1 after

50 h oxidation (**Fig. 3b**), suggesting that the difference in oxidation rate between HEA1 and HEA2 is negligible. Even after 1000 h oxidation, no TGO rumpling and spallation can be observed for the HEA2. Y/Hf-rich oxides at TGO grain boundaries are also seen on HEA2 after oxidation (**Fig. 3c-e**), which is similar to the observations on HEA1. Meanwhile, the TGO remains exclusively Al_2O_3 after 1000 h oxidation (**Fig. 3f-g**). The surface roughness of the TGO is merely ~0.98 μm after 1000 h oxidation, which is much lower than that of HEA1 after 50 h oxidation (**Fig. 3h**). In short, the TGO rumpling of HEA2 is well inhibited via lowering Cr content and the oxidation resistance of HEA2 is significantly improved.

Based on the above results, the TGO growth rates of two alloys are comparable and no interface imperfections are formed in either of the alloys after oxidation at 1200 ℃. Therefore, the difference in oxidation resistance between HEA1 and HEA2 is attributed to TGO rumpling. According to the established theories formulated in previous works [26-29], TGO rumpling is predominantly determined by the thermal mismatch stress and growth stress in TGO, the creep resistance of alloy substrate, the phase transformation of alloy substrate. Since there is no repeated generation and release of thermal mismatch stress during the isothermal oxidation, the effect of thermal mismatch stress on the TGO rumpling can be neglected. The growth stress (σ_g) is predominantly generated by the lateral growth of TGO, which can be estimated from the residual stress in TGO by assuming no stress relaxation in cooling. Our calculations (see **supplementary material** section 1 in detail) show that the growth stress of TGO is almost the similar for HEA1 (~0.13 GPa) and HEA2 (~0.15 GPa). Furthermore, the TGOs on the two alloys show similar thickness and predominantly columnar grain microstructure with nearly same average width of the columnar grains (~1μm) after 50 h oxidation (**Fig. S2c**), indicating that the TGO growth shares the same kinetics and is primarily governed by inward oxygen diffusion [30-31]. Overall, the similar TGO growth kinetics and microstructure result in similar TGO growth stress for the HEA1and HEA2.

The TGO rumpling is controlled by not only the TGO growth stress, but also the creep

resistance of HEA substrate [32-33]. To achieve force balance during the oxidation process, the compressive growth stress within the growing oxide must be balanced by a tensile stress within the metal substrate. The tensile stress induces creep deformation of the metal substrate, initiating simultaneous rumpling of both the TGO and metal substrate. For a flat alloy substrate, the force balance requires that [34]

$$\sigma_m h_m + 2\sigma_g h_{ox} = 0 \quad (1)$$

$$\sigma_m = -\frac{2\sigma_g h_{ox}}{h_m} \quad (2)$$

where the σ_m and h_m are the stress and thickness of metal substrate, h_{ox} denotes the thickness of TGO. The tensile stress calculated from **Eq. (1)** and **Eq. (2)** is ~0.32 MPa for HEA1 after 50 h oxidation at 1200 ℃. Such a low tensile stress is unlikely to induce the creep deformation of HEA1 substrate [10] and, therefore, has limited influence on TGO rumpling.

After assessing and ruling out all the above-mentioned factors, we have identified that the remaining significant difference between HEA1 and HEA2 is the microstructure of their Al-depleted layers. Evidenced by the TKD analysis (**Fig. 2i**) and XRD patterns (**Fig. 4a**), the microstructure of the Al-depleted layer in HEA1 comprises a σ phase matrix and BCC precipitates while the Al-depleted layer in HEA2 is single FCC phase. Based on the DSC cooling curve (**Fig. 4b**), the formation temperature of σ phase is around 700 ℃, which suggests that the σ phase is not a thermodynamically favorable phase at high temperature. However, the σ phase is found in the Al-depleted layer of HEA1 after 1200 ℃ oxidation by air cooling, suggesting the occurrence of possible phase transformation from the BCC phase (stable phase at 1200 ℃) to σ phase in Al-depleted layer during the air cooling. The phase transformation is accompanied by a volume change, which induces mechanical strain and results in rumpling. The following sections will provide further microstructural characterizations for understanding the phase transformation, calculate the strain induced the phase transformation and validate our hypothesis on phase transformation induced rumpling by experiment.

To understand the phase transformation in detail, we conducted TEM analysis on the

microstructure of the Al-depleted layer in HEA1 after 50 h oxidation at 1200 ℃ (**Fig. 4c-e**). The nanoscale phases in the Al-depleted layer are identified as B2 precipitates embedded within the σ phase matrix. STEM-EDS mapping (**Fig. 4c**) indicates that the σ phase matrix is rich in CrCoFe, while the B2 precipitates are rich in AlNi. **Table. 2** shows the chemical composition of Al-depleted layer in HEA1. Clearly, the σ phase has a similar composition with the A2 phase (**Table. 1** and **Table. 2**), indicating the σ phase probably originates from the A2 phase in the HEA1 substrate. It is well known that the mobility and content of Cr is important for the thermodynamic driving force for formation of the σ phase [35]. As the Al atoms diffuse from the Al-depleted layer to the TGO during the oxidation process, other atoms (e.g. Cr and Fe) migrate to compensate for the vacancies left by Al atoms [36]. Consequently, the mobility of Cr and Fe atoms is enhanced by this phenomenon, which may result in the σ phase formation in the Al-depleted layer. As for the HEA2, only single FCC phase is found in the Al-depleted layer. The mobility of Cr and Fe atoms in FCC phase is significantly lower than that in A2 phase [37], which contributes to the difference in Cr diffusion behavior between the Al-depleted layer of HEA1 and HEA2. Eventually, no TGO rumpling is observed in the HEA2 even after 1000 h at 1200 ℃ oxidation.

Furthermore, we calculate the volume change and its associated strain during the transformation to understand its effect on TGO rumpling. The volume change, ΔV, induced by the A2 to σ phase transformation is given by

$$\Delta V = V_{A2} - V_{\sigma} = N\left(\frac{a_{A2}^3}{N_{A2}} - \frac{a_{\sigma}^2 \times c_{\sigma}}{N_{\sigma}}\right) \quad (3)$$

where N is an arbitrary total number of atoms in A2 and σ phase; N_{A2} and N_{σ} are the number of atoms in the A2 and σ unit cell ($N_{A2} = 2$ and $N_{\sigma} = 30$), respectively; a_{A2} is the lattice parameters of the cubic A2 phase, a_{σ} and c_{σ} are the lattice parameters of the tetragonal σ phase (**Table. 3** [38]). Substituting ΔV by **Eq. (4)**, the linear strain, ε_{tr}, generated by the volume change can be estimated by

$$\varepsilon_{tr} = \frac{1}{3}\frac{\Delta V}{V_{A2}} = \frac{1}{3}\left(\frac{15a_{A2}^3 - a_\sigma^2 \times c_\sigma}{15a_{A2}^3}\right) \quad (4)$$

By inserting the values in **Table. 3** to **Eq. (4)**, ε_{tr} is calculated to be ~1.2%. The magnitude of the strain is comparable to the martensitic transformation strain (~0.7%) in β-(Ni,Pt)Al bond coat [39]. Furthermore, we use the Finite Element Method (FEM) to determine the distribution of von mises stress across the TGO, the Al-depleted layer and the underlying substrate in response to the phase transformation strain in the Al-depleted layer at the phase transformation temperature (~700 ℃). The calculated stress in Al-depleted layer is approximately 700 MPa (see **supplementary material** section 2 in detail), which is significantly higher than the yield stress of HEA1 at 700 ℃ (~450MPa) [40]. Therefore, the presence of this phase transformation in the Al-depleted layer of the HEA1 induces the stress at the TGO/substrate interface and plastic deformation of metal substrate, eventually cause the TGO rumpling during the cooling process.

To test our hypothesis regarding the effect of this phase transformation on TGO rumpling of HEA1, we conducted an identical oxidation test of HEA1 at 1200 ℃ but used water quenching for cooling to completely suppress the phase transformation. Our *in-situ* surface temperature measurements in cooling have confirmed that the cooling rate in water quenching within the temperature range of phase transformation is 50 times higher than that in air cooling (see section 3 in **supplementary material**). No TGO rumpling or spallation is observed from the surface of the HEA1 quenched in water after 50 h oxidation at 1200 ℃ (**Fig. 5a-b**). The absence of rumpling after water quenching is further confirmed by the smooth and continuous TGO/metal interface (**Fig. 5c-e**). XRD pattern and TEM analysis show that the Al-depleted layer of HEA1 after water quenching comprises an A2 matrix and B2 precipitates (**Fig. 5f-g**), which confirms the lack of A2 to σ phase transformation in cooling. This experiment validates our hypothesis that the phase transformation is the main reason for TGO rumpling of HEA1.

In conclusion, we have found that the equimolar AlCoCrFeNi HEA undergoes TGO rumpling after oxidation at 1200 ℃, which results in TGO cracking and spallation. TGO rumpling is primarily attributed to the A2 to σ phase transformation and its associated strain within the Al-depleted layer during cooling. Reducing the Cr content in the AlCoCrFeNi HEA can significantly reduce rumpling and improve the oxidation resistance by inhibiting the A2 to σ phase transformation. Fast water quenching also mitigate TGO rumpling by freezing the phase transformation. The findings provide scientific guidance for designing oxidation resistant AlCoCrFeNi high entropy alloys or coatings with higher durability.

Acknowledgements

This work was supported by National Natural Science Foundation of China (No. 52201082, No. 52102072 and No. 51971139) and Shanghai Sailing Program (No. 22YF1419200). This work is also sponsored by Chenguang Program supported by Shanghai Education Development Foundation and Shanghai Municipal Education Commission (No. 21CGA10).

References

[1] N.P. Padture, M. Gell, E.H. Jordan, Thermal barrier coatings for gas-turbine engine applications, Science (80-.). 296 (2002) 280–284.

[2] S. Salam, P.Y. Hou, Y. D. Zhang, H. F. Wang, C. Zhang, Z.G. Yang, Compositional effects on the high-temperature oxidation lifetime of MCrAlY type coating alloys, Corros. Sci. 95 (2015) 143–151.

[3] J.L. Smialek, Invited Review Paper in Commemoration of Over 50 Years of Oxidation of Metals: Alumina Scale Adhesion Mechanisms: A Retrospective Assessment, Oxid. Met. 97 (2022) 1–50.

[4] A. Huang, Y. Chen, Z. Zhang, J. Shen, L. Li, X. Liu, H. Zhang, J. Lu, X. Zhao, Effect of Al content on the oxidation behavior of NiCoCrAlYHf alloys at 1100 ℃, Corros. Sci. 222 (2023) 111417.

[5] M.J. Pomeroy, Coatings for gas turbine materials and long term stability issues, Mater. Des. 26 (2005) 223–231.

[6] J. Lu, Y. Chen, H. Zhang, L. He, R. Mu, Z. Shen, X. Zhao, F. Guo, Y/Hf-doped $Al_{0.7}$CoCrFeNi

high-entropy alloy with ultra oxidation and spallation resistance at 1200 ℃, Corros. Sci. 174 (2020) 108803.

[7] B. Cantor, I.T.H. Chang, P. Knight, A.J.B. Vincent, Microstructural development in equiatomic multicomponent alloys, Mater. Sci. Eng. A. 375–377 (2004) 213–218.

[8] J.-W. Yeh, S.-K. Chen, S.-J. Lin, J.-Y. Gan, T.-S. Chin, T.-T. Shun, C.-H. Tsau, S.-Y. Chang, Nanostructured High-Entropy Alloys with Multiple Principal Elements: Novel Alloy Design Concepts and Outcomes, Adv. Eng. Mater. 6 (2004) 299–303.

[9] Y. Lu, Y. Dong, H. Jiang, Z. Wang, Z. Cao, S. Guo, T. Wang, T. Li, P.K. Liaw, Promising properties and future trend of eutectic high entropy alloys, Scr. Mater. 187 (2020) 202–209.

[10] Y. Zhang, T.T. Zuo, Z. Tang, M.C. Gao, K.A. Dahmen, P.K. Liaw, Z.P. Lu, Microstructures and properties of high-entropy alloys, Prog. Mater. Sci. 61 (2014) 1–93.

[11] Y. Li, P. Shi, M. Wang, Y. Yang, Y. Wang, Y. Li, Y. Wen, W. Ren, N. Min, Y. Chen, Y. Guo, Z. Shen, T. Zheng, N. Liang, W. Lu, P.K. Liaw, Y. Zhong, Y. Zhu, Unveiling microstructural origins of the balanced strength–ductility combination in eutectic high-entropy alloys at cryogenic temperatures, Mater. Res. Lett. 10 (2022) 602–610.

[12] Y.F. Kao, S.K. Chen, T.J. Chen, P.C. Chu, J.W. Yeh, S.J. Lin, Electrical, magnetic, and Hall properties of $Al_xCoCrFeNi$ high-entropy alloys, J. Alloys Compd. 509 (2011) 1607–1614.

[13] H.P. Chou, Y.S. Chang, S.K. Chen, J.W. Yeh, Microstructure, thermophysical and electrical properties in $Al_xCoCrFeNi$ ($0 \leqslant x \leqslant 2$) high-entropy alloys, Mater. Sci. Eng. B Solid-State Mater. Adv. Technol. 163 (2009) 184–189.

[14] Y.F. Kao, T.D. Lee, S.K. Chen, Y.S. Chang, Electrochemical passive properties of $Al_xCoCrFeNi$ (x = 0, 0.25, 0.50, 1.00) alloys in sulfuric acids, Corros. Sci. 52 (2010) 1026–1034.

[15] L. Li, J. Lu, X. Liu, T. Dong, X. Zhao, F. Yang, F. Guo, $Al_xCoCrFeNi$ high entropy alloys with superior hot corrosion resistance to Na_2SO_4 + 25% NaCl at 900 °C, Corros. Sci. 187 (2021) 1–14.

[16] J. Lu, Y. Chen, H. Zhang, L. Li, L. Fu, X. Zhao, F. Guo, P. Xiao, Effect of Al content on the oxidation behavior of Y/Hf-doped AlCoCrFeNi high-entropy alloy, Corros. Sci. 170 (2020) 108691.

[17] J. Lu, L. Li, Y. Chen, X. Liu, X. Zhao, F. Guo, P. Xiao, Y-Hf co-doped AlCoCrFeNi high-entropy alloy coating with superior oxidation and spallation resistance at 1100 °C, Corros. Sci. 182 (2021) 109267.

[18] J. Lu, Y. Chen, H. Zhang, N. Ni, L. Li, L. He, R. Mu, X. Zhao, F. Guo, Y/Hf-doped AlCoCrFeNi

high-entropy alloy with ultra oxidation and spallation resistance, Corros. Sci. 166 (2020) 108426.

[19] J. Lu, Y. Chen, L. Li, H. Zhang, X. Zhang, X. Zhao, An in-situ oxide-dispersion-strengthened AlCoCrFeNiY high-entropy alloy composite coating prepared by AC-HVAF with superior oxidation and spallation resistance, Compos. Part B Eng. 265 (2023) 110933.

[20] T.M. Butler, M.L. Weaver, Investigation of the phase stabilities in AlNiCoCrFe high entropy alloys, J. Alloys Compd. 691 (2017) 119–129.

[21] M.G. Jo, J.Y. Suh, M.Y. Kim, H.J. Kim, W.S. Jung, D.I. Kim, H.N. Han, High temperature tensile and creep properties of CrMnFeCoNi and CrFeCoNi high-entropy alloys, Mater. Sci. Eng. A. 838 (2022) 142748.

[22] J. Lu, H. Zhang, L. Li, A. Huang, X. Liu, Y. Chen, X. Zhang, F. Guo, X. Zhao, Y-Hf co-doped $Al_{1.1}CoCr_{0.8}FeNi$ high-entropy alloy with excellent oxidation resistance and nanostructure stability at 1200°C, Scr. Mater. 203 (2021) 114105.

[23] A. Munitz, S. Salhov, S. Hayun, N. Frage, Heat treatment impacts the micro-structure and mechanical properties of AlCoCrFeNi high entropy alloy, J. Alloys Compd. 683 (2016) 221–230.

[24] C. Zhang, F. Zhang, S. Chen, W. Cao, Computational thermodynamics aided high-entropy alloy design, Jom. 64 (2012) 839–845.

[25] B.A. Pint, Experimental observations in support of the dynamic-segregation theory to explain the reactive-element effect, Oxid. Met., 45 (1996) 1–37.

[26] L. Yang, Z. Zou, Z. Kou, Y. Chen, G. Zhao, X. Zhao, F. Guo, P. Xiao, High temperature stress and its influence on surface rumpling in NiCoCrAlY bond coat, Acta Mater. 139 (2017) 122–137.

[27] D.S. Balint, J.W. Hutchinson, An analytical model of rumpling in thermal barrier coatings, J. Mech. Phys. Solids. 53 (2005) 949–973.

[28] D.J. Jorgensen, A. Suzuki, D.M. Lipkin, T.M. Pollock, Bond coatings with high rumpling resistance: Design and characterization, Surf. Coatings Technol. 300 (2016) 25–34.

[29] H.E. Evans, Stress effects in high temperature oxidation of metals, Int. Mater. Rev. 40 (1995) 1–40.

[30] D.J. Young, High temperature oxidation and corrosion of metals, Elsevier, 2008.

[31] K.P.R. Reddy, J.L. Smialek, A.R. Cooper, ^{18}O Tracer studies of Al_2O_3 scale formation on NiCrAl alloys, Oxid. Met. 17 (1982) 429–449.

[32] H.E. Evans, M.P. Taylor, Creep relaxation and the spallation of oxide layers, Surf. Coatings

Technol. 94–95 (1997) 27–33.

[33] M.T. Hernandez, A.M. Karlsson, M. Bartsch, On TGO creep and the initiation of a class of fatigue cracks in thermal barrier coatings, Surf. Coat. Technol. 203 (2009) 3549–3558.

[34] J.A. Nychka, C. Pullen, M.Y. He, D.R. Clarke, Surface oxide cracking associated with oxidation-induced grain boundary sliding in the underlying alloy, Acta Mater. 52 (2004) 1097–1105.

[35] C.-C. Hsieh, W. Wu, Overview of Intermetallic Sigma (σ) Phase Precipitation in Stainless Steels, ISRN Metall. 2012 (2012) 1–16.

[36] N. Birks, G.H. Meier, F.S. Pettit, Introduction to the High Temperature Oxidation of Metals, Cambridge Univ Pr, 2013 (2006).

[37] L. Duprez, B.C. De Cooman, N. Akdut, Redistribution of the substitutional elements during σ and χ phase formation in a duplex stainless steel, Steel Res. 72 (2001) 311–316.

[38] W.R. Wang, W.L. Wang, J.W. Yeh, Phases, microstructure and mechanical properties of $Al_xCoCrFeNi$ high-entropy alloys at elevated temperatures, J. Alloys Compd. 589 (2014) 143–152.

[39] M.W. Chen, M.L. Glynn, R.T. Ott, T.C. Hufnagel, K.J. Hemker, Characterization and modeling of a martensitic transformation in a platinum modified diffusion aluminide bond coat for thermal barrier coatings, Acta Mater. 51 (2003) 4279–4294.

[40] K.R. Lim, K.S. Lee, J.S. Lee, J.Y. Kim, H.J. Chang, Y.S. Na, Dual-phase high-entropy alloys for high-temperature structural applications, J. Alloys Compd. 728 (2017) 1235–1238.

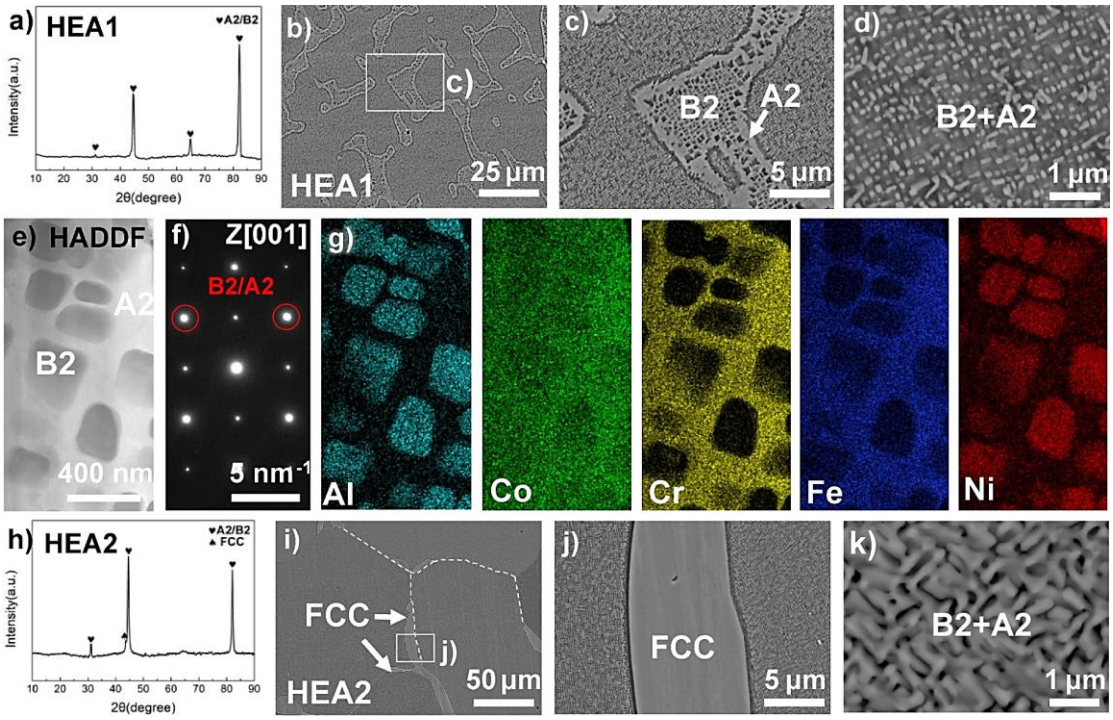

Fig. 1 Microstructural analysis of HEA1 and HEA2: a) XRD pattern of HEA1. The peaks of A2 and B2 overlap due to their similar lattice parameters; b) low magnification BSE image of HEA1; c) and d) high magnification BSE image, showing the nano-structured A2/B2 phase of HEA1 in bright and dark regions, respectively; e) STEM-HADDF image and g) EDS mapping of the bright region in HEA1 with f) a SAED pattern along [001] zone axis, showing the element distribution in A2 and B2; h) XRD pattern of HEA2; i) low magnification BSE image of HEA2; j) and k) high magnification BSE images of HEA2, showing the FCC phase and nano-structured B2+A2 phase. (The white dash line in Fig. 1i denotes the grain boundaries of HEA2).

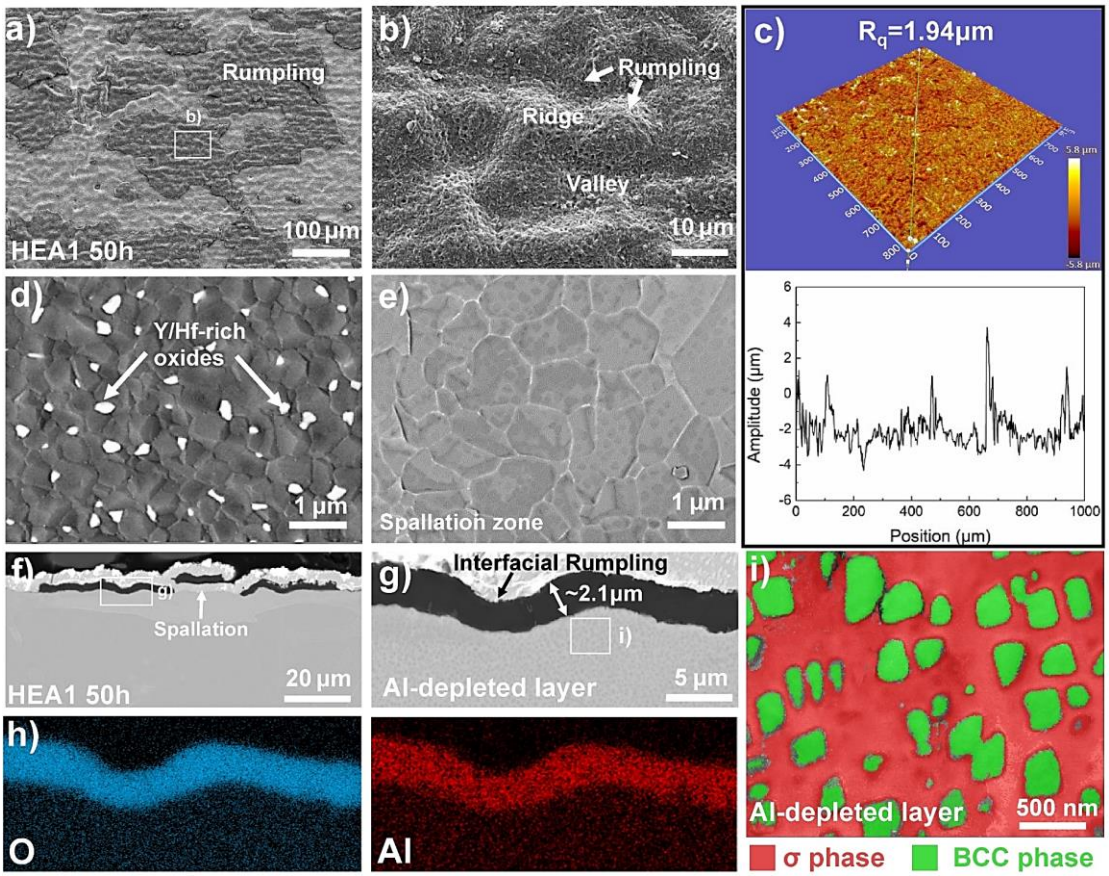

Fig. 2 Surface and cross-sectional morphology of TGO formed on the HEA1 after 50 h oxidation at 1200 ℃ : a-b) SE images of TGO surface revealing TGO rumpling, cracking and spallation; c) profilometer image and height profile (green line) of HEA1; d) BSE image of TGO surface, showing the distribution of Y/Hf-rich oxides; e) BSE image of the exposed metal surface, showing the TGO imprints; f-g) BSE images and h) EDS mapping of alloy cross-section, showing the interface rumpling; i) A TKD phase-contrast map of the Al-depleted layer, which shows a dual-phase microstructure that comprises a continuous σ matrix and nanoscale BCC precipitates.

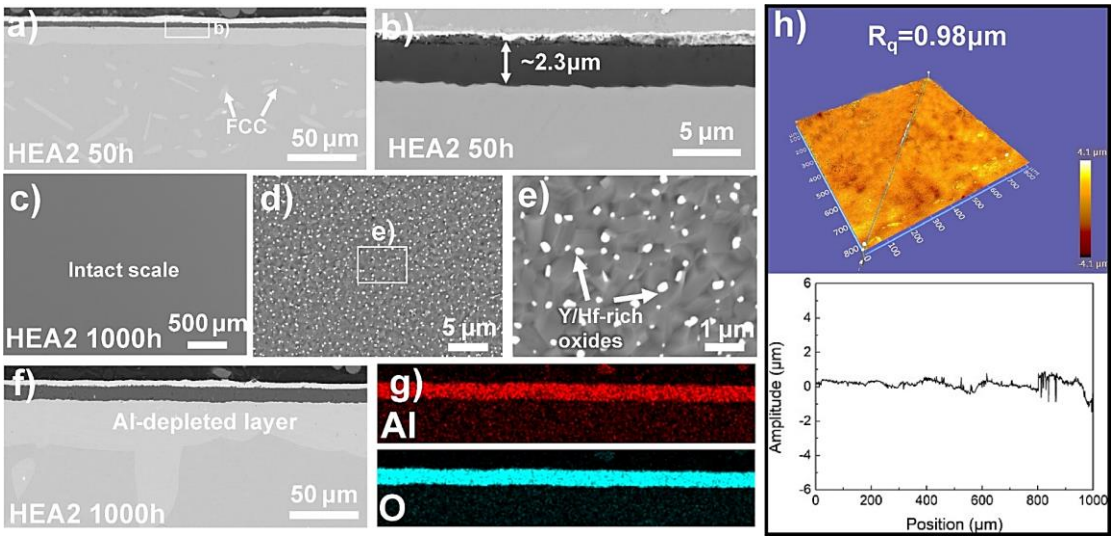

Fig. 3 Surface and cross-sectional morphology of TGO formed on the HEA2 after 50 h and 1000 h oxidation at 1200 ℃: a-b) BSE images of cross-section after 50 h oxidation, showing no interfacial rumpling; c-e) BSE images of TGO surface after 1000 h oxidation, showing no TGO spallation; f) BSE images and g) EDS mapping of cross-section after 1000 h oxidation, showing no interfacial rumpling; f) Profilometer image and height profile (green line) after 1000 h oxidation.

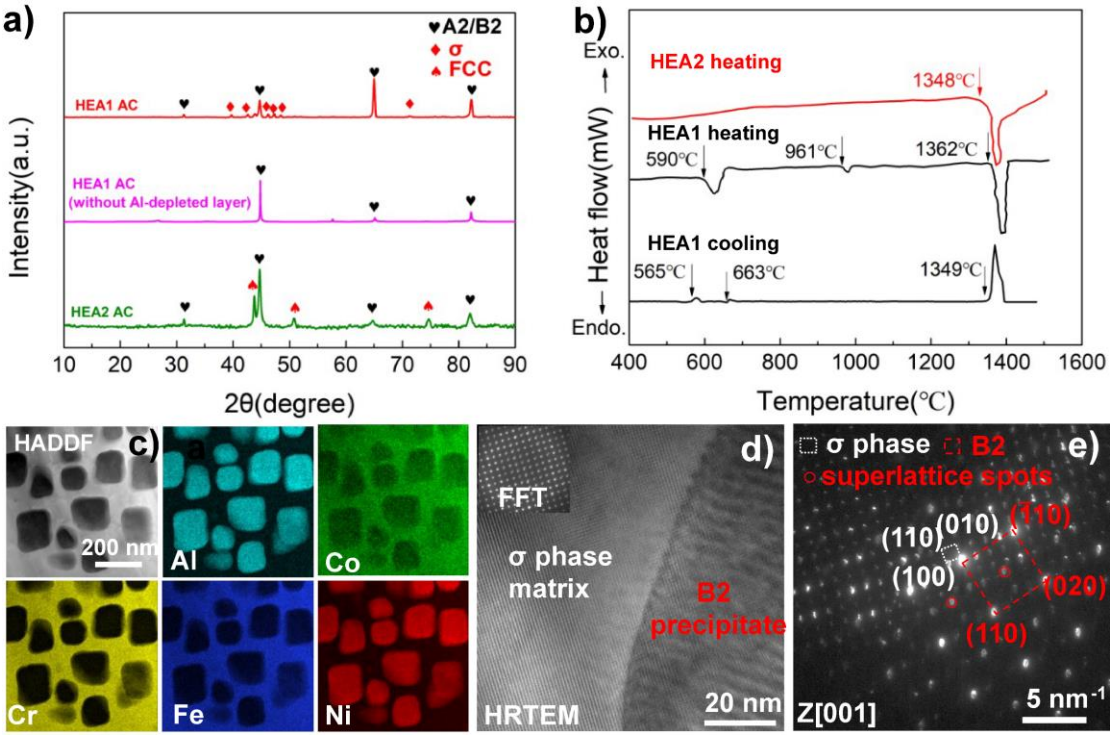

Fig. 4 Phase transformation and microstructural analysis of HEA1 and HEA2: a) XRD patterns of HEA1 and HEA2 with different cooling process after 50 h oxidation at 1200 ℃ and the TGO is removed before the XRD test (AC: Air cooling); b) DSC heating and cooling curves of HEA1 and HEA2 with 20 ℃/min heating rate and 10 ℃/min cooling rate, showing the phase transformation temperature; c) STEM-EDS image of the Al-depleted layer in HEA1 after 50 h oxidation at 1200 ℃; d) HRTEM image of the Al-depleted layer in HEA1 after 50 h oxidation at 1200 ℃; e) SAED pattern showing the bright and dark phases, indexed as [001] zone of σ and B2 phases (the red circles indicate the superlattice spots of the B2 phase).

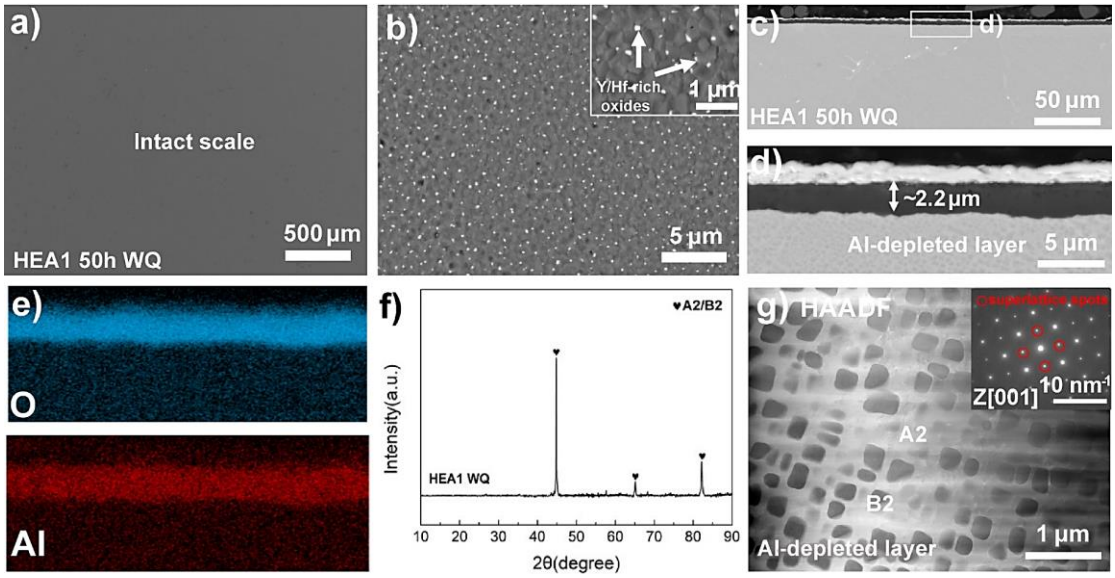

Fig. 5 Surface and cross-sectional morphology of TGO formed on the HEA1 after 50 h oxidation at 1200 ℃ followed by water quenching: a-b) BSE images of TGO surface after 50 h oxidation, showing no rumpling or spallation; c-d) BSE images and e) EDS mapping of cross-section of HEA1, showing no interfacial rumpling; f) XRD pattern of HEA2 after 50 h oxidation by water quenching and the TGO is removed before test; g) STEM-DF image, showing the microstructure of the Al-depleted layer (the inset shows the SAED pattern of B2/A2 phase along the [001] zone axis).

Table 1 Composition of A2 and B2 in HEA1 quantified from TEM-EDS point analysis (standard deviations are based on measurement results from 5 points).

Elements	HEA1	
	A2 phase (at.%)	B2 phase (at.%)
Al	3.8±0.2	30.7±0.7
Co	19.8±0.8	21.3±0.6
Cr	41.3±0.3	3.6±0.4
Fe	28.1±0.2	12.9±0.3
Ni	7.0±0.5	31.5±0.7

Table 2 Composition of σ and B2 in Al-depleted layer of HEA1 after 50 h oxidation at 1200 ℃ quantified from TEM-EDS point analysis (standard deviations are based on measurement results from 5 points).

Elements	Al-depleted layer of HEA1	
	σ phase (at.%)	B2 precipitate (at.%)
Al	1.4±0.1	29.4±1.7
Co	20.6±0.9	20.2±0.6
Cr	42.1±1.2	5.4±0.4
Fe	30.5±1.5	15.0±0.3
Ni	5.4±0.5	30.0±0.7

Table 3 Lattice parameters of σ and A2 phase in Al-depleted layer of HEA1 after 50 h oxidation at 1200 ℃ quantified from TEM-SAED and reference [38].

Phases	Lattice parameters (Å)	
	a	c
σ phase	8.87	4.79
A2 phase	2.97	\